TECHNICAL ARTICLE

Al-12Si Alloy Fabricated Via Selective Laser Melting: Residual Stress and Microstructural Factors after Heat Treatment

Seonghwan Park, Sang Hoon Kim, Jiyong Park, and Eunkyung Lee

This study investigated the correlation between the residual stress and microstructural factors, such as the thermal expansion mismatch of Al and Si, Si solid solubility, and dislocation density, in Al-12Si alloys. As-built Al-12Si alloys produced via selective laser melting were solution heat treated at 540 °C for 1, 7, and 26 h, followed by water quenching. Here, the as-built Al-12Si alloy exhibited the highest residual stress in the Al matrix owing to the large temperature gradient and high Si solid solubility. After heat treatment for 1 h, the residual stress abruptly decreased to -4 ± 2 MPa. With an increase in the solution time, the residual stress improved to -15 ± 2 and -21 ± 2 MPa for Al-12Si alloys heat treated for 7 and 26 h, respectively, owing to the further Al matrix expansion, Si solid solubility, and dislocation density. Additionally, the relationship between the residual stress, microstructure, and coefficient of thermal expansion was experimentally elucidated. This study's findings reveal the residual stress behavior of Al-12Si alloys by collectively considering the microscale factors and are expected to be relevant for future research on improving the prediction accuracy of residual stresses of Al-Si alloys.

1. Introduction

In an attempt to improve the fuel efficiency and reduce emissions, automobile and aerospace industries have increased the use of aluminum, which is a lightweight material (Ref 1). Al (Al-Si) alloys with high strength-to-weight ratios, suitable fluidity, and excellent corrosion resistance have been widely used in a variety of car components, such as cylinder blocks, cylinder heads, pistons, and valve lifters (Ref 2-4). Al alloys are used to manufacture automotive components through high-pressure die-casting (HPDC) (Ref 5). This process can be used to produce complex and high-volume parts. Additionally, the

recent rapid development of selective laser melting (SLM), which is a promising powder bed fusion additive manufacturing technology, has attracted widespread interest in automobile and aerospace industries because of its significant potential for application in the near-net-shape fabrication of Al-Si alloys with improved mechanical properties, complex component geometries, and material usage efficiencies (Ref 6, 7). However, residual stresses and casting defects, such as hot tearing, porosity, and blistering, can occur during the HPDC process (Ref 6, 8). Additionally, the additive manufacturing process generates residual stresses owing to large thermal gradients (Ref 9, 10). The generated residual stresses, possessing a high magnitude, deteriorate mechanical properties, such as the fatigue life, corrosion resistance, and fracture toughness, leading to unexpected failures (Ref 11-13). To enhance the mechanical properties and ensure the safety of materials and structural components, the relaxation and accurate prediction of residual stress are of paramount importance. The residual stress can be mitigated through solution heat treatment and annealing (Ref 14, 15). Lombardi et al. (Ref 14) showed that the residual stress significantly decreased with an increase in the initial heat-treatment time. With a further increase in the heat-treatment time, the stress became relatively constant. Additionally, simulations have been used to predict the residual stresses. However, the internal stress values predicted using simulations, particularly in complex mechanical parts, are frequently inaccurate. This is because the simulations only consider the residual stresses caused by the difference in cooling rates inside and outside of the material; however, the microstructure parameters also substantially affect the internal stresses. Therefore, considering these factors are imperative to accurately predict the residual stresses. To include these parameters in the simulation, the dependence of residual stress behavior on the microstructural factors should be thoroughly understood.

Seonghwan Park and **Jiyong Park**, Advanced Joining and Additive Manufacturing R&D Department, Korea Institute of Industrial Technology, 156 Gaetbeol-ro, Yeonsu-gu, Incheon 21999, Republic of Korea; and Department of Convergence Manufacturing System Engineering, University of Science and Technology (UST), 217 Gajeong-ro, Yuseong-gu, Daejeon 34113, Republic of Korea; **Sang Hoon Kim**, Additive Manufacturing Innovation Agency, Korea Institute of Industrial Technology, Siheung, Gyeonggi-do 15014, Republic of Korea; and **Eunkyung Lee**, Interdisciplinary Major of Maritime AI Convergence, Department of Ocean Advanced Materials Convergence Engineering, Korea Maritime and Ocean University, Busan 49112, South Korea. Contact e-mails: j.park@kitech.re.kr and elee@kmou.ac.kr.

Residual stresses, which are defined as stresses that remain in a material irrespective of external forces and thermal gradients, can be classified according to the scale. Type I stresses develop at a scale larger than the grain size. Types II and III stresses vary at the microscale depending on the secondary phases, grain size, dislocation, mismatch of the coefficient of thermal expansion (CTE) values of the Al matrix and Si particle, and lattice strain (Ref 11, 13, 16-20). The influence of the secondary phases on the residual stresses of the Al-Si-Mn-Mg alloy AA365 (Silafont-36) at different cooling rates was evaluated. The compressive residual stresses were demonstrated to be affected by the secondary phases, including β' and β''. Additionally, the reduction in the residual stress is due to the plastic deformation caused by the fracture of the brittle intermetallic phases (Ref 16). Considering the correlation between the grain size and residual stresses, a large number of grain boundaries in the alumina/zirconia composite reduce the level of residual stresses owing to spreading relaxation (Ref 17). Węglewski et al. (Ref 18) investigated the effects of the grain size on the thermal residual stresses in sintered Cr/Al_2O_3 and showed that the composite with a fine grain size exhibited a lower residual stresses than that with a coarse grain size. Based on a previous study (Ref 19), the microdefects and inhomogeneity in the microstructure increase the dislocation density, enhancing the residual stress. In the case of thermal expansion mismatch, when a material is cooled to room temperature, the magnitude disparity between the CTE values of the matrix and particles generates residual stresses. Rosenthal et al. (Ref 20) reported that residual stresses are formed owing to the mismatch between the CTE values of the Al matrix and Si particles, with values of 21.5×10^{-6} and 2.6×10^{-6} K^{-1}, respectively. The correlation of the residual stress with the lattice strain obtained using the x-ray diffraction (XRD) analysis is shown in Eq. 1 (Ref 21).

$$\sigma_\emptyset = \frac{E}{(1-v)\sin^2\varphi}\left(\frac{d_\varphi - d_0}{d_0}\right) \qquad \text{(Eq 1)}$$

where $\sigma_\emptyset$, E, v, d_φ, and d_0 denote the residual stress, elastic modulus, Poisson's ratio, measured spacing of the diffraction plane, and the lattice spacing, respectively. Considering Eq. 1, the residual stress is strongly dependent on the lattice strain (Ref 22, 23). The magnitude of the lattice strain is primarily determined by the presence of dislocations and substitutional atoms (Ref 24, 25). Considering substitutional atoms, the introduction of a small solute atom in the solid solution matrix reduces the lattice constant, whereas that of a larger solute atom increases the lattice parameter (Ref 26). Based on the literature (Ref 27), the radius of an Al atom (0.14318 nm) is larger than that of a Si atom (0.11758 nm), which suggests that increasing the solid solubility of Si reduces the Al lattice parameters. In other words, as the solubility of Si increases in the Al matrix, the Al lattice strain increases, contributing to the increase in the residual stresses. Based on the aforementioned studies, several microstructural factors significantly affect the level of residual stress. Therefore, several previous studies have explored the relationship between the residual stresses of Al alloys and various microstructural parameters. However, a clear understanding of the residual stress behavior by collectively considering these parameters is essential to determine the internal stresses caused by the simultaneous action of the forces. However, no comprehensive study of the residual stress behavior, particularly for the Al-12Si alloy, has been conducted thus far by collectively considering the microstructure parameters.

This study aims to comprehensively determine the correlation between the microstructural effects, such as the thermal expansion mismatch of Al and Si, Si solid solubility, and dislocation density, and the residual stress of the Al-12Si alloy. Additionally, the effects of the microstructural factors and residual stresses on the CTE were experimentally analyzed. The results reveal the residual stress behavior by collectively considering the microscale factors and can serve as important guidelines for future studies to improve the prediction accuracy of the residual stresses of Al-Si alloys using simulations.

2. Experimental

2.1 SLM Process

Cubic samples ($23 \times 23 \times 23$ mm) were fabricated via SLM using a ProX300 machine with a laser power of 200 W, scanning speed of 1400 mm/s, layer thickness of 40 μm, laser spot size of 80 μm,, and hatch distance of 70 μm. The samples were processed using a zigzag laser scanning pattern with a rotation of 90° between successive layers. No pre-heating was applied to the building platform. The chemical composition of Al-12Si powder was determined using energy-dispersive x-ray spectroscopy (EDS) as 12.2% Si, 0.08% Fe, 0.01% Zn, 0.01% Ti, and Al balance.

2.2 Heat Treatment and Residual Stress Measurement

The as-built Al-12Si alloys were solution heat treated at 540 °C for different times of 1, 7, and 26 h in an electric furnace, followed by water quenching to increase the Si solid solubility in the Al matrix (Ref 28), to obtain three sets of Al-12Si alloy samples. After the solution heat treatment, XRD (D/MAX 2500 V L/PC, Rigaku) measurements were performed using Cu-Kα radiation ($\lambda = 1.54$ Å) at 40 kV and 30 mA. The diffraction angle (2θ) was varied from 20 to 120° in increments of 0.001°. The residual stress measurement was conducted on the top-view microstructure of the as-built and the heat-treated samples. The (420) Al phase was selected for the residual stress analysis.

2.3 Analysis of Microstructure, Mechanical Property, and CTE

The as-built and heat-treated Al-12Si samples were polished using SiC polishing paper (up to #2400), a 0.25 μm diamond suspension, and a 0.04 μm colloidal suspension to obtain a mirror-like surface, followed by etching with the Keller's reagent (190 mL H_2O + 5 mL HNO_3 (65%) + 3 mL HCl (32%) + 2 mL HF (40%)). The top-view microstructure of these samples was analyzed using optical microscopy (OM; Nikon ECLIPSE LV150N) and field-emission scanning electron microscopy (FE-SEM; MIRA) equipped with an EDS instrument (EDAX) at an accelerating voltage of 15.0 kV. The pore fraction was studied using iSolution DT software in conjunction with OM. The number of Si particles per unit area was measured using image analysis software (ImageJ). Furthermore, for each sample, a minimum of 15 different fields were examined. A nanoindenter (Anton Paar) with a maximum indentation load of 7.5 mN and average indentations per sample of > 30 was used to measure the nanohardness. To obtain the inverse pole figure, grain size, and dislocation density of the as-

built and heat-treated Al-12Si specimens, an electron backscatter diffraction (EBSD) system (JSM-7200F) with a step size of 0.4 μm and an accelerating voltage of 20.00 kV were employed; the ATEX software was used for the analysis (Ref 29). Dilatometry measurements were performed in an argon atmosphere from room temperature to 700 K at a heating rate of 5 K/min using a thermomechanical analyzer (TMA; TMA Q400).

2.4 Geometrically Necessary Dislocation (GND) Analysis

GNDs are stored dislocations induced by the geometrical disorientation in crystals. The increase in the disorientation determines the amount of the GND or plastic strain accumulation. In terms of single or multiple glides in two-dimensional and three-dimensional objects, the Nye tensor component should be considered (Ref 30). The elastic distortion (U_e) can be estimated using local elastic curvature values derived from EBSD analysis based on Eq. 2 (Ref 31).

$$\alpha = \text{Curl } U_e \qquad (\text{Eq 2})$$

U_e comprises an elastic strain tensor (ε_e) and a rotation strain tensor (ω_e). Therefore, the localized strain can be described as follows.

$$\alpha = \text{Curl } \varepsilon_e + \text{Curl } \omega_e \qquad (\text{Eq 3})$$

The elastic strain tensor has a negligible contribution and can therefore be excluded from the calculations (Ref 32). Accordingly, Eq. 3 can be modified to Eq. 4.

$$\alpha = \text{Curl } \omega_e \qquad (\text{Eq 4})$$

where ω denotes the function of the elastic curvature components (k), which relies on the cumulative Burgers vector of the same sign, that is, nb (n = number of dislocation and b = Burgers vector) (Ref 31). The GND density is described as:

$$\rho_{\text{GND}} = \frac{\alpha}{b} \qquad (\text{Eq 5})$$

where ρ_{GND} and b denote the localized dislocation density and Burgers vector, respectively. Therefore, Nye tensor components were employed for calculating the GND after obtaining lattice rotation from the EBSD map using the ATEX software. Additionally, the GND density was calculated as the average misorientation ($< 5°$) with neighboring grains (Ref 9).

3. Results and Discussion

3.1 Characterization of Microstructure and Nanohardness

The top-view microstructures of the as-built and heat-treated Al-12Si samples are shown in Fig. 1. The high-magnification SEM image of the as-built sample in Fig. 1(a) exhibits two distinctive zones, namely the coarse grain zone and fine grain zone, with different grain sizes. This novel microstructure was ascribed to the fact that heat from the overlapping scan lines and the creation of subsequent layers affected the Al microstructure produced by SLM, which led to localized heating and coarsened the microstructure (Ref 33). The eutectic structure is composed of cellular Al grains surrounded by many small spherical Si particles (60-250 nm). This fine microstructure is caused by the high cooling rate of the SLM process,

which restrains the growth of the particles (Ref 35). For the heat-treated samples, Si particles and pores are observed, as shown in Fig. 1(b), (c), and (d). As the heat-treatment time increases, the number of Si particles in the Al matrix decreases with increase in Si particle size, owing to the coalescence of adjacent Si particles and Ostwald ripening (Ref 33), as shown in Fig. 2. Additionally, the pore fraction in the samples heat treated for 1, 7, and 26 h is 0.197%, 0.327%, and 0.821%, respectively, as shown in Fig. 3, indicating that the pore fraction increases with the solution time. The increase in the percentage of pores with prolonged heat treatment time is because high-temperature and long-term preservation promote the diffusion of elements and the accumulation of porosity (Ref 34).

The average nanohardness of the as-built sample was 1.74 GPa. After heat treatment, the nanohardness of the specimens heat treated for 1, 7, and 26 h is 1.5, 0.95, and 0.88 GPa, respectively, as observed in Fig. 4. The strength of the as-built Al-12Si sample can be ascribed to solid solution and grain boundary strengthening. First, the high cooling rates led to excessive Si solid solubility in the Al matrix, strengthening the as-built sample. Second, the fine Si particles induced by the excessive cooling rates in the SLM process served as grain boundaries to impede dislocation motion, improving the hardness of the as-built sample (Ref 36). Figure 5 shows the average grain sizes of the as-built and heat-treated Al-12Si alloys obtained from the EBSD measurements. As the solution heat-treatment time increases, the hardness values decrease, as shown in Fig. 4. From Fig. 5(d), (f), and (h), the average grain sizes are 4.62, 4.73, and 5.62 μm for the samples heat treated for 1, 7, and 26 h, respectively. Therefore, the increase in the grain size weakens the Hall–Petch effect, reducing the hardness.

3.2 Residual Stress Analysis

Figure 6 shows the residual stresses in the Al matrix of the as-built and heat-treated samples. The stresses in all the samples exhibited negative values, implying that the Al matrix exhibited compressive residual stress. The residual stresses of the as-built sample and samples heat treated for 1, 7, and 26 h were -37 ± 1.2, -4 ± 2, -15 ± 2, and -21 ± 2 MPa, respectively. The as-built sample exhibited the highest residual stress because an excessively large temperature gradient existed during the SLM process (Ref 10). For the heat-treated samples, the internal stresses increased with increase in solution heat-treatment time. The residual stress is affected by two main factors. The first is the mismatch of the CTE values of Al (21.5×10^{-6}) and Si (2.6×10^{-6} K^{-1}) (Ref 20). When the Al matrix is expanded further, it shrinks more during the cooling process, creating a significantly larger thermal contraction mismatch between Al and Si and leading to a high residual stress. Zhu et al. (Ref 37) indicated that when the number of Si particles was reduced, the restraining effect of the Si particles on the Al matrix decreased, increasing the CTE. The number of Si particles shown in Fig. 2 was reduced with heat-treatment time increased, indicating that the thermal expansion might increase with increase in heat-treatment time. Therefore, the increase in the residual stresses with the extended heat treatment time can be explained by the additional thermal expansion caused by the decrease in the number of Si particles. To verify that the Al matrix expands further as the heat-treatment time increases, the GND maps derived from the
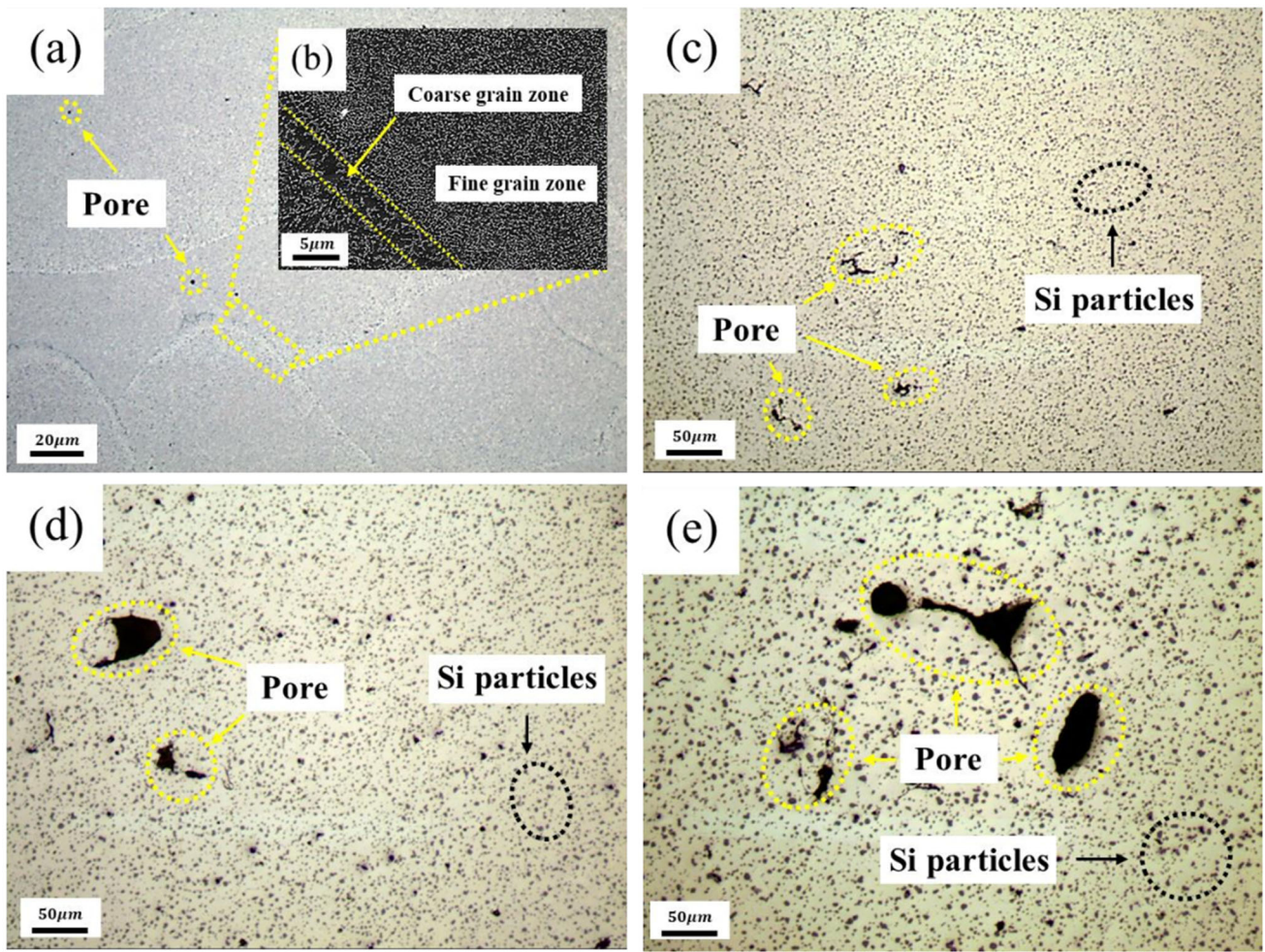
Fig. 1 Microstructure of top view of as-built and heat-treated Al-12Si alloys: (a) optical micrograph and (b) the inset is the high magnification SEM image of as-built sample; (c), (d), (e) optical micrographs for heat-treated samples for 1, 7, and 26 h respectively
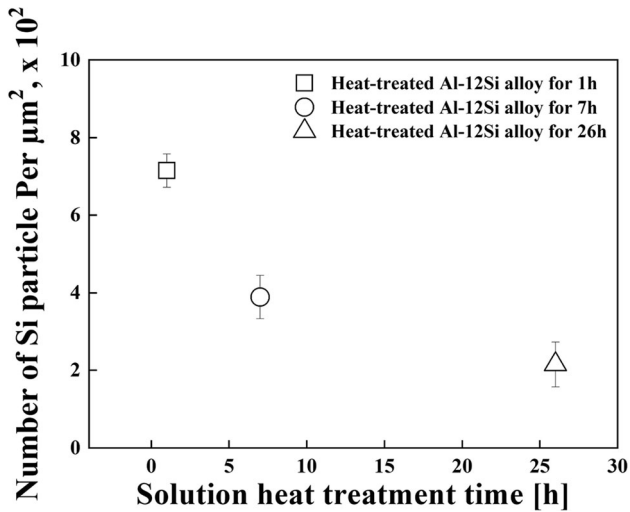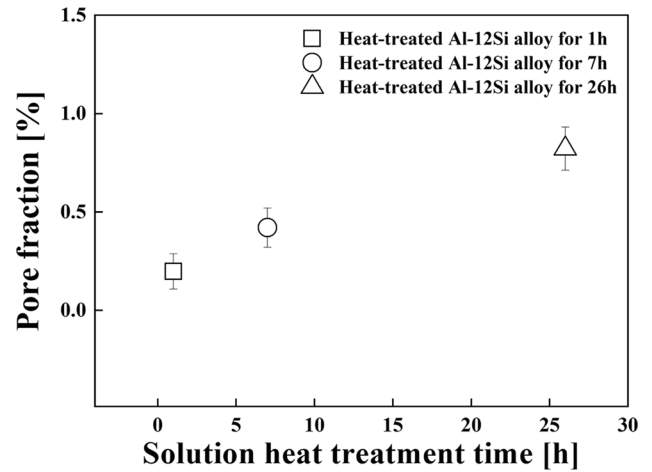

Fig. 2 Number of Si particle as a function of solution heat treatment time of heat-treated Al-12Si alloys based on the OM images shown in Fig. 1.

Fig. 3 Pore fraction as a function of solution heat treatment time of heat-treated Al-12Si alloys based on the OM images shown in Fig. 1.

EBSD data for the heat-treated Al-12Si samples are presented in Fig. 7. The GND map of the as-built sample could not be obtained because of the relatively high number of zero solutions. In the as-built sample, high residual stresses generated by a large temperature gradient during the SLM process triggered lattice distortion, affecting the Kikuchi patterns. As shown in Fig. 7(a), (b), and (c), the average GND densities of

the heat-treated samples are 0.21×10^{-14}, 0.42×10^{-14}, and 0.55×10^{-14} m^{-2} for the sample heat treated for 1, 7, and 26 h, respectively, indicating that the GND densities increase with increase in solution time. The formation of GNDs can be attributed to the difference in the CTE values of Al and Si (Ref 38). Therefore, as the heat-treatment time increased, the number of Si particles decreased, further expanding and subsequently shrinking the Al matrix, thereby generating a relatively high dislocation density and residual stresses. Therefore, the GND map analysis results support the conjecture that the Al matrix expands further with the prolongation of the heat treatment, thereby increasing the residual stresses.

Moreover, the increase in the dislocation density could be ascribed to the improvement of the Si solid solubility, which hinders the dislocation movement. To calculate the solubility of the Si solid in the Al matrix, the XRD peaks are analyzed, as shown in Fig. 8. All diffraction peaks can be attributed to either Al or Si. The peak position of the Al (420) lattice plane of the as-built sample shifts to a higher 2θ angle than those of the heat-treated samples. Additionally, as the heat-treatment time increases, the peaks of the heat-treated specimens shift to higher 2θ angles. Based on the peak positions of the Al (420) lattice plane, the interplanar crystal spacings of the as-built and heat-treated samples were calculated using $d_{hkl} = \frac{a}{\sqrt{h^2+k^2+l^2}}$, where h, k, and l are the Miller indices of the lattice plane, and a is the lattice parameter. The interplanar spacings of the as-built sample and samples heat treated for 1, 7, and 26 h were 0.088986, 0.090534, 0.090530, and 0.090514 nm, respectively, indicating that each sample had a different interplanar spacing. Furthermore, based on the calculated internal spacings, the Al lattice parameters of the as-built sample and samples heat treated for 1, 7, and 26 h were estimated as 0.39796, 0.404884, 0.404866, and 0.404792 nm, respectively. As mentioned previously, an increase in the solid solubility of Si decreases the Al lattice parameter (Ref 27). To measure the solid
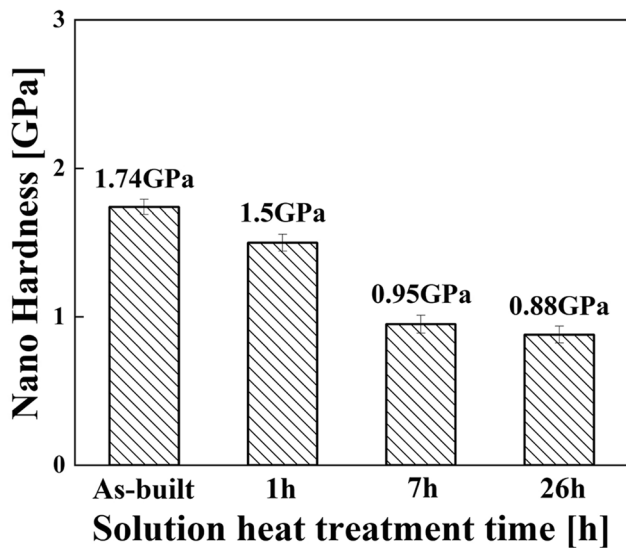

Fig. 4 Nano-hardness as a function of solution heat treatment time of as-built and heat-treated Al-12Si alloys
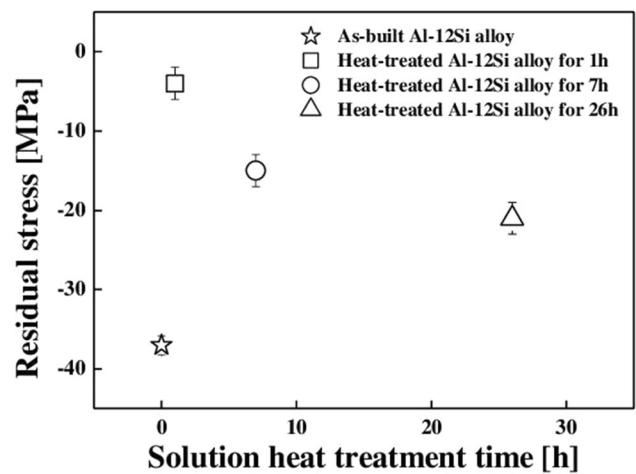

Fig. 6 Residual stress as a function of solution heat treatment time of as-built and heat-treated Al-12Si alloys
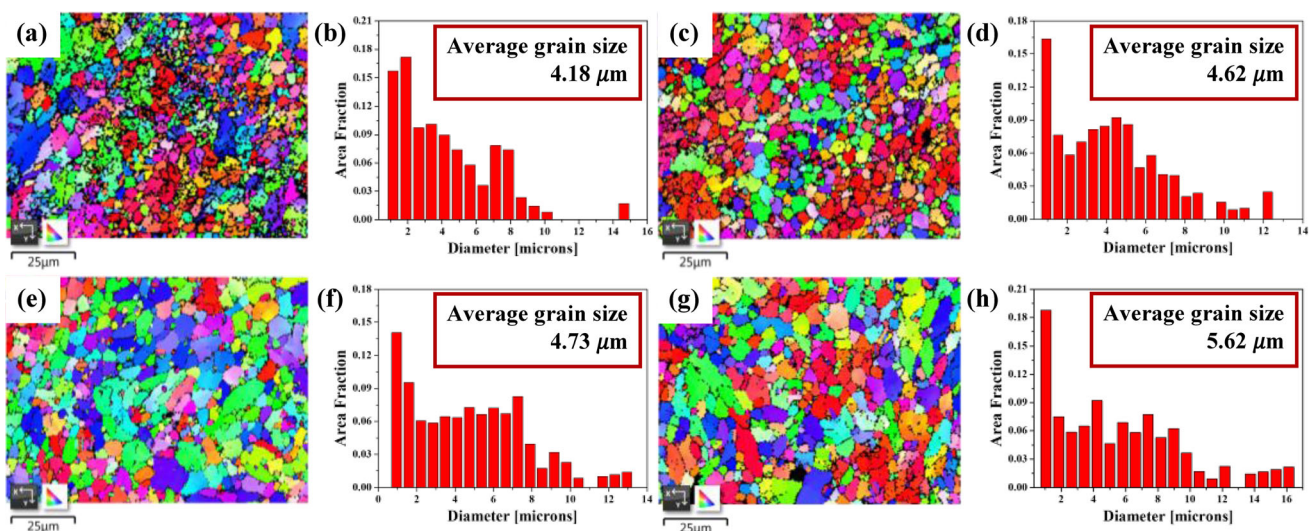

Fig. 5 EBSD images of the microstructure of as-built and heat-treated Al-12Si alloys: (a), (b) as-built Al-12Si alloy; (c), (d) heat-treated Al-12Si alloy for 1 h; (e), (f) heat-treated Al-12Si alloy for 7 h; (g), (h) heat-treated Al-12Si alloy for 26 h
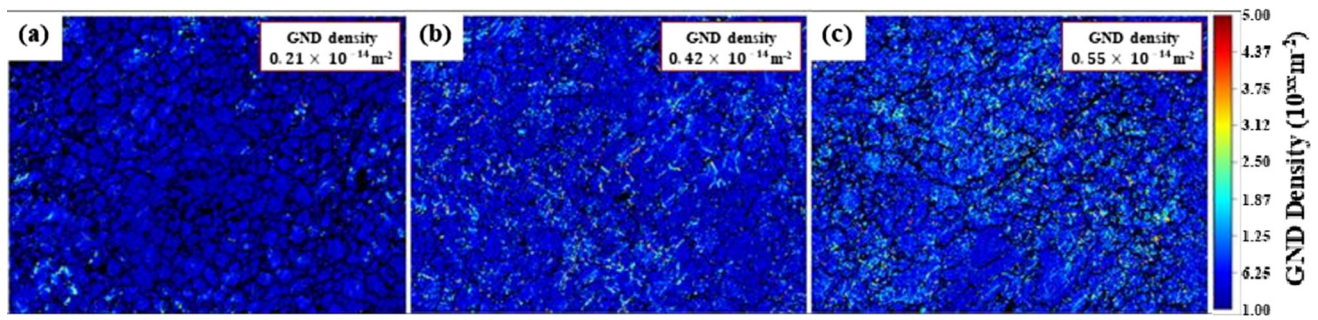
Fig. 7 GND maps for the heat-treated Al-12Si alloys constructed using EBSD data: (a) 1 h; (b) 7 h; (c) 26 h
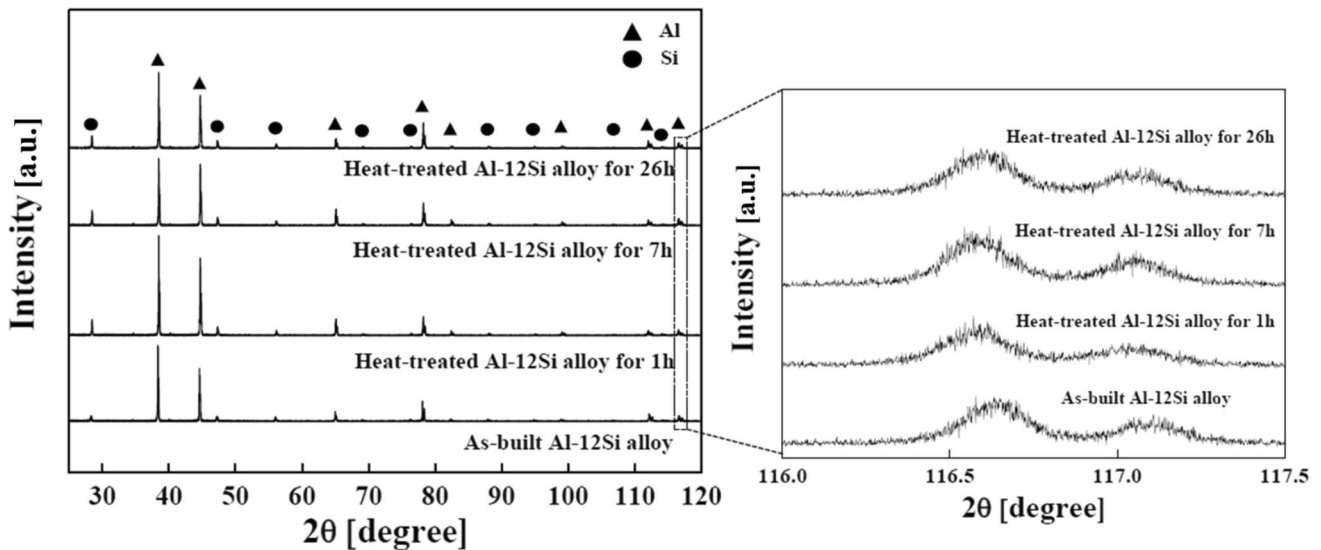

Fig. 8 The XRD patterns of as-built and heat-treated Al-12Si alloys produced by SLM

solubility of Si in the Al matrix of the as-built and heat-treated samples, the solid-solution model proposed by Bendijk et al. was used (Ref 39, 40).

$$a = 0.40491 - 0.0174X_{\text{si}}^2 \qquad \text{(Eq 6)}$$

where a and X_si represent the Al lattice parameter and the Si atomic fraction in the Al matrix, respectively. Based on Eq. 6, the solid solubility of Si in the as-built sample and samples heat treated for 1, 7, and 26 h are calculated as 6.32, 0.38, 0.5, and 0.83 at.%, respectively, as shown in Fig. 9. The solid solubility of Si in the as-built sample considerably exceeded the maximum Si solubility of 1.8 at.% at the eutectic temperature (Ref 41). This supersaturated Si solubility contributed to the high cooling rate. After solution heat treatment for 1 h, the Si solid solubility decreased rapidly from 6.32 to 0.38 at.%. This is because upon heat treatment, the supersaturated Si atoms were expelled from the Al matrix to form Si particles, decreasing the solubility. Li et al. (Ref 33) reported that after heat treatment at 500 °C for 30 min, the Si content decreased to the equilibrium state. This implies that heat treatment at 540 °C for 1 h could be sufficient to reduce the solubility of the Si solid to the equilibrium level. For the heat-treated samples, the solubility of Si increased with increase in solution heat-treatment time. Therefore, based on the calculation of the Al lattice parameters and Si solid solubilities, the increase in the
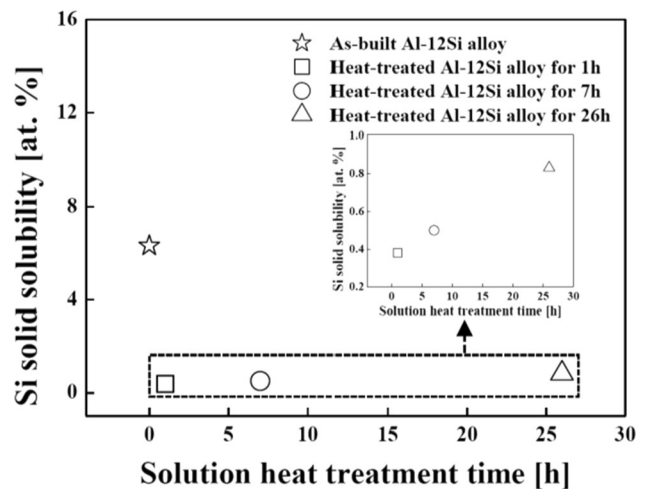

Fig. 9 Si solid solubility of as-built and heat-treated Al-12Si alloys as a function of solution heat treatment time

dislocation density with the increase in the heat-treatment time could be explained by the extension of Si solid solubility.

Second, the microstrain caused by variations in the interplanar crystal spacing (induced by solid solution and dislocations) increases with an increase in the residual stress (Ref 42). The Williamson–Hall method was used to calculate the

microstrain based on the XRD results. This method assumes that the overall peak broadening is due to both grain refinement and microstrain broadening and is expressed as (Ref 43):

$$\frac{\beta_{hkl}\cos\theta_{hkl}}{\lambda} = \frac{1}{D^{W\cdot H}} + \frac{4\varepsilon^{WH}\sin\theta_{hkl}}{\lambda} \qquad (\text{Eq 7})$$

where λ is the wavelength of Cu K$_\alpha$ radiation (0.154 nm), and β_{hkl} is the integral breadth. $D^{W\cdot H}$ and $\varepsilon^{W\cdot H}$ represent the grain size and microstrain, respectively. However, previous studies have demonstrated that when the grain size exceeds 100 nm, the effect of $D^{W\cdot H}$ on the peak broadening is insignificant (Ref 42, 44). For the as-built and heat-treated samples, the average grain sizes are generally higher than 4 μm, as shown in Fig. 5, indicating that $1/D^{W\cdot H}$ can be ignored. Figure 10 shows plots drawn with $4\sin\theta_{hkl}$ on the x-axis and $\beta_{hkl}\cos\theta_{hkl}$ along the y-axis for the as-built sample and Al-12Si alloy samples heat treated for 1, 7, and 26 h. The as-built sample exhibits the maximum slope ($\varepsilon^{W\cdot H} = 0.000919$), as shown in Fig. 10(a). This is because the excessive Si solid solubility (6.32 at.%) resulted in severe Al lattice distortions, enhancing the microstrain that corresponded to the residual stress. After the solution heat treatment for 1 h, the slope decreases abruptly from 0.000919 to 0.000214 owing to the radical decrease in the Si solubility from 6.32 to 0.38 at.%, as shown in Fig. 10(b). With increase in solution time, the microstrain increases from 0.000214 (sample heat treated for 1 h) to 0.000295 (sample heat treated for 7 h) and 0.000445 (sample heat treated for 26 h), as shown in Fig. 10(c) and (d), respectively. This enhancement is because of the increase in the Si solid solubility from 0.38 to 0.5 and 0.83 at.% as the solution heat-treatment time is increased. In other words, the amelioration of the residual stresses with increase in heat-treatment time could be ascribed to the improvement in the microstrain caused by the increase in the Si solubility. Furthermore, with increase in heat-treatment time, the average GND densities of the Al-12Si alloys heat treated for 1, 7, and 26 h increase to 0.21×10^{-14}, 0.42×10^{-14}, and 0.55×10^{-14} m^{-2}, respectively (Fig. 7), thereby increasing the microstrain. In other words, the increase in the residual stresses with the prolongation of the heat treatment could be explained by the enhancement in the microstrain induced by the increase in the dislocation densities. Therefore, the increase in the Si solid solubility and dislocation density with increase in heat-treatment time resulted in an enhancement of the residual stress.

3.3 CTE Analysis

The variation in the CTE values of the as-built and heat-treated Al-12Si alloys is shown in Fig. 11. In the temperature range of 300-500 K, the CTE of the as-built Al-12Si alloy is lower than that of the heat-treated Al-12Si alloys. However, the
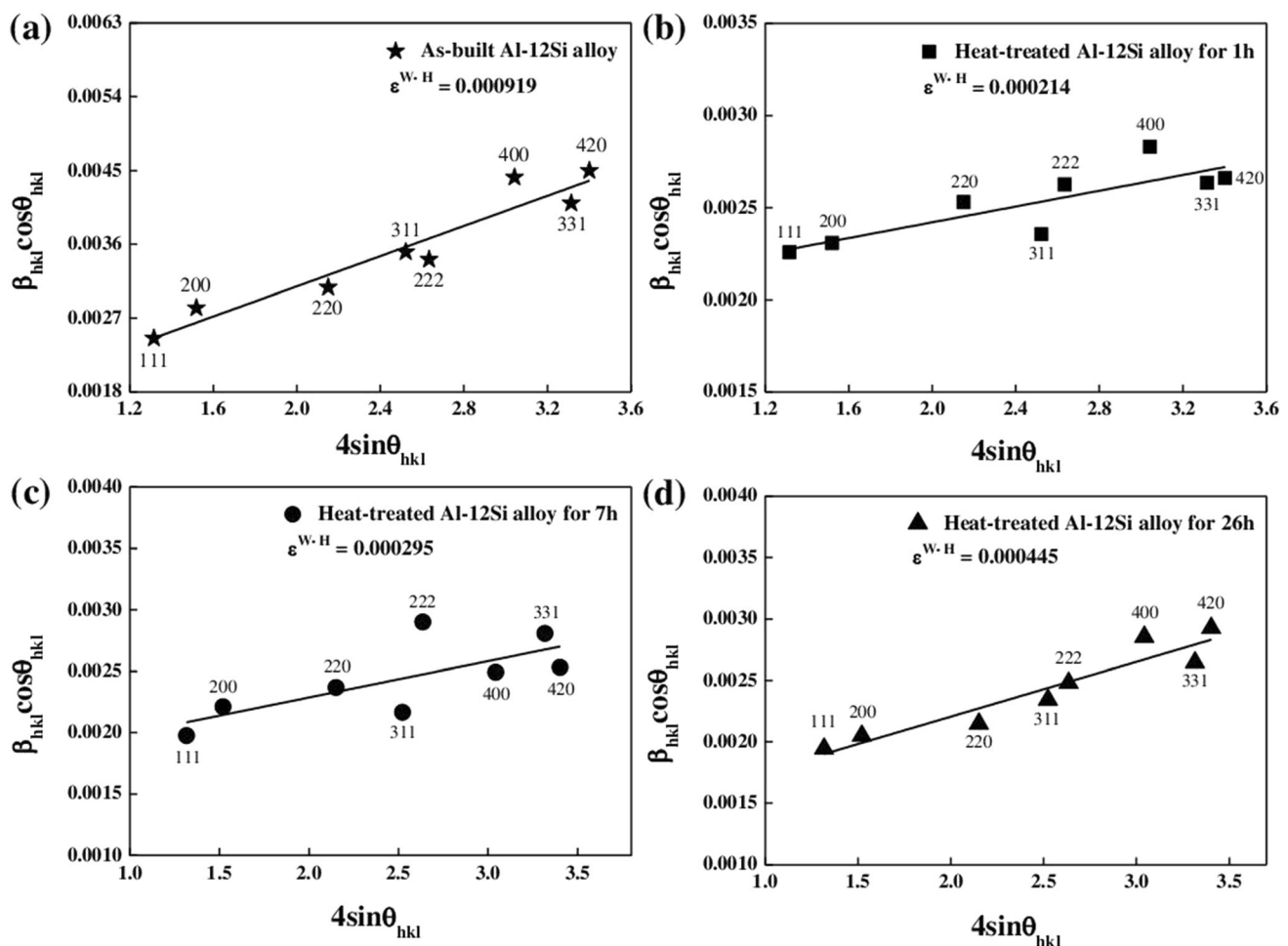

Fig. 10 (a) Williamson–Hall plots for as-built Al-12Si alloy; (b) heat-treated Al-12Si alloy for 1 h; (c) heat-treated Al-12Si alloy for 7 h; (d) heat-treated Al-12Si alloy for 26 h
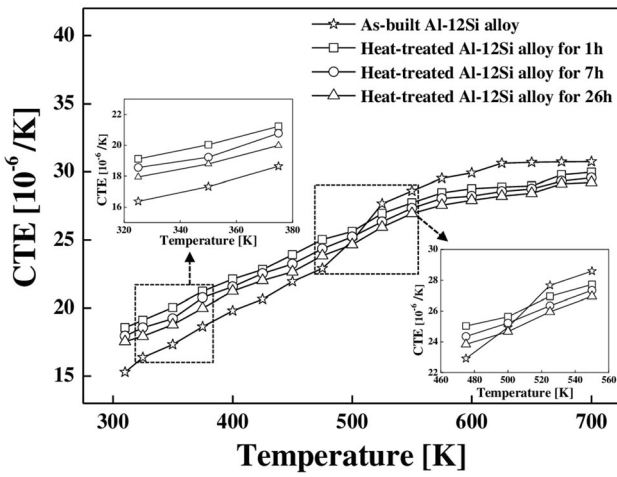
Fig. 11 CTE curves of as-built and heat-treated Al-12Si alloys, insets are the enlarged curves in the temperature range from 320 to 380 K and from 460 to 560 K

CTE of the as-built sample increases significantly from 22.912×10^{-6} K^{-1} at 475 K to 27.665×10^{-6} K^{-1} at 525 K, which is higher than that of the heat-treated samples at 525 K, as shown in Fig. 11. In contrast, an unconventional CTE peak is not observed for the heat-treated samples. Additionally, as the solution heat-treatment time increased, the CTE values of the heat-treated samples indicated no further thermal expansion. The factors affecting the CTE are complicated and include the residual stress, number of Si particles, porosity, and Si solid solubility. Hence, a precise investigation of the CTE values of the as-built and heat-treated samples considering only one determining factor is difficult. The internal stress (300-373 K), number of Si particles, and solid solubility of Si in the Al matrix accounted for this trend below 500 K. First, based on a previous study (Ref 37), the residual stress could constrain the expansion of the matrix, thereby decreasing the CTE. In the temperature range from 300 to 373 K, the CTE of the as-built sample was lower than those of the other samples because of the high residual stress induced by the large temperature gradient and high Si solid solubility. Second, when the number of Si particles decreases, the restraint by Si particles on the Al matrix declines, decreasing the CTE (Ref 37). As shown in Fig. 1(a), the number of Si particles in the as-built sample is higher than that in the samples subjected to solution heat treatments for different times. In other words, a large number of these particles restrained the expansion of the Al matrix, thereby reducing the CTE of the as-built sample. Finally, an increase in the Si solid solubility in the Al matrix has a negative effect on the CTE (Ref 45). The CTE (α) is given by the variation in the lattice parameter.

$$\alpha = \frac{1}{a_0} \cdot \frac{da}{dT} \tag{Eq 8}$$

where a_0 is the intrinsic lattice parameter; dT represents the temperature change; da is the change in the lattice parameter with dT; and a is the lattice parameter, expressed as:

$$a = a_0 + \frac{\Delta a}{\Delta C} C \tag{Eq 9}$$

where C is the concentration related to the heat-treatment solution and is described as:

$$C = A e^{-\Delta H/RT} \tag{Eq 10}$$

By combining Eq. 9 and 10, the CTE can be expressed as:

$$\alpha = \frac{1}{a_0} \cdot \frac{da_0}{dT} + \frac{1}{a_0}\left(\frac{\Delta a}{\Delta C}\right) A e^{-\frac{\Delta H}{RT}}\left(\frac{\Delta H}{RT^2}\right) \tag{Eq 11}$$

where $\frac{1}{a_0} \cdot \frac{da_0}{dT}$ represents the intrinsic lattice expansion, and $\frac{1}{a_0}\left(\frac{\Delta a}{\Delta C}\right) A e^{-\frac{\Delta H}{RT}}\left(\frac{\Delta H}{RT^2}\right)$ is the contribution of the variations in the solute concentration. A, R, and ΔH have values of 994, 8.314 J/mol·K, and 45,500 J/mol, respectively (Ref 46, 47). Based on the solute contribution, which is the second term in Eq. 11, when Δa is negative, $\frac{1}{a_0}\left(\frac{\Delta a}{\Delta C}\right) A e^{-\frac{\Delta H}{RT}}\left(\frac{\Delta H}{RT^2}\right)$ will be negative. In other words, an increase in the Si solid solubility in Al has a negative effect on the CTE (Ref 27). As previously mentioned, the Al lattice parameter of the as-built sample is 0.39796 nm. Using the calculated values of the Al lattice constant and the Si solid solubility, the solute contribution to the CTE in the as-built sample was estimated to be approximately -1.94×10^{-6} K^{-1} at 350 K. This implies that among the analyzed samples, the as-built sample has the highest Si solute contribution, resulting in a negative effect on the CTE. These three factors explain the reasons for the lower CTE of the as-built sample than those of the other samples. Above 500 K, an unconventional CTE peak is observed for the as-built sample. This peak is due to the rejection and precipitation of the Si atoms from the Al matrix during the heating process. It has been reported that Si has a diamond cubic structure with a lattice equal to 5.430 Å and eight atoms per unit cell. By contrast, Al has a face-cubic-center (FCC) structure with a 4.049 Å lattice with 4 atoms per unit cell. The precipitation of diamond-cubic-structured Si results in an atomic volume 21.3% higher than that in the FCC-structured Al solid solution, generating an unconventional CTE peak (Ref 47, 48). For the heat-treated samples, as the solution heat-treatment time increased, the CTE values decreased. The reduction in the CTE values can be attributed to three factors: the residual stress, Si solid solubility, and porosity. As mentioned earlier, the residual stress affects the expansion of the matrix. With increase in heat-treatment time, the residual stresses increased because of further Al matrix expansion and the changes in the Si solid solubility and dislocation density. In other words, the increase in the residual stresses explains the reduction in the CTE values of the heat-treated Al-12Si alloys in the temperature range of 300-373 K with the prolonged heat treatment. Additionally, as the heat-treatment time increased, the Si solid solubilities increased, resulting in a negative effect on the CTE. Furthermore, as the porosity increased, a certain portion of Al expanded into the pores, restricting the increase in the CTE (Ref 46). The porosity fraction in the heat-treated samples increases from 0.197% to 0.327% and 0.821% as the solution heat-treatment time increases, as shown in Fig. 3, indicating that the growth of the pores interrupts the increase in the CTE. Hence, the decrease in the CTE of the heat-treated specimens with increase in solution-treatment time could be attributed to the residual stress, solid solubility of Si, and porosity. No distinct CTE peak is observed because of the expulsion of Si atoms from the Al matrix to precipitate after the solution heat treatment.

4. Conclusion

This study elucidated the effects of microstructural factors on the residual stresses of Al-12Si alloys. Furthermore, the relationship between the microstructural factors and residual stresses as well as CTE was experimentally investigated. The conclusions drawn from this study are as follows.

1. The two distinctive zones with different grain sizes observed in the as-built sample were attributed to overlapping scan lines and the creation of subsequent layers. The ultrafine eutectic Si particles became slightly coarser with an increase in the solution heat-treatment time owing to Oswald ripening and the coalescence of adjacent Si particles. Additionally, the pore fraction increased with increase in heat-treatment time. The average nanohardness of the as-built specimen was the highest (1.74 GPa) among that of the samples analyzed in this study. This can be explained by two factors: solid-solution strengthening and Hall–Petch strengthening. For the heat-treated samples, the increase in the grain size contributed to the reduction in the nanohardness with increase in solution heat-treatment time.

2. The XRD results suggested that among the analyzed samples, the as-built sample exhibited the highest residual stress in the Al matrix (-37 ± 1.2 MPa) owing to the large temperature gradient and high Si solid solubility (6.32 at.%). After heat treatment for 1 h, the residual stresses in the Al matrix decreased abruptly to -4 ± 2 MPa. With an increase in solution time, the residual stress increased to -15 ± 2 (Al-12Si alloy heat treated for 7 h) and -21 ± 2 MPa (Al-12Si alloy heat treated for 26 h). The enhancement of the residual stresses was attributed to increasing Al matrix expansion, Si solid solubility, and dislocation density.

3. For the as-built sample, below 500 K, the internal stress (300-373 K), constraining effects of Si on the expansion of the Al matrix, and supersaturated Si solubility were deemed as the reasons for a lower CTE than that of the samples subjected to heat treatment for different times. Above 500 K, the CTE of the as-built sample was higher than that of the heat-treated samples owing to the precipitation of Si particles from the Al matrix. For the heat-treated specimens, with increase in solution time, the CTE values decreased because of the residual stress, Si solid solubility, and increase in the porosity.

The current study demonstrated the residual stress behavior of Al-12Si alloys by considering various microstructural parameters, such as the thermal expansion mismatch of Al and Si, Si solid solubility, and dislocation density. The findings of this study will help elucidate the residual stress mechanism under the action of the microscale factors and therefore are relevant for scientific research to enhance the prediction accuracy of the residual stresses in Al-Si alloy with simulations.

Conflict of interest

The authors have no relevant financial or non-financial interests to disclose.

References

1. C. Ahn, I. Jo, C. Ji, S. Cho, B. Mishra, and E. Lee, Creep Behavior of High-Pressure Die-Cast AlSi10MnMg Aluminum Alloy, *Mater. Charact.*, 2020, **167**, p 110495

2. G. Moon and E. Lee, Combined Effects of Optimized Heat Treatment and nickel Coating for the Improvement of Interfacial Bonding in Aluminum–Iron Alloys Hybrid Structures, *Appl. Sci.*, 2021, **11**(4), p 1501

3. A.M.A. Mohamed, F.H. Samuel, A.M. Samuel, and H.W. Doty, Influence of Additives on the Impact Toughness of Al-10.8% Si Near-Eutectic Cast Alloys, *Mater. Design*, 2009, **30**(10), p 4218–4229

4. M. Dias, R. Oliveira, R. Kakitani, N. Cheung, H. Henein, J.E. Spinelli, and A. Garcia, Effects of Solidification Thermal Parameters and Bi Doping on Silicon Size, Morphology and Mechanical Properties of Al-15wt.% Si-32 wt.% Bi and Al-18wt.% Si-32 wt.% Bi alloys, *J. Mater. Res. Technol.*, 2020, **9**(3), p 3460–3470

5. K.T. Chiang, N.M. Liu, and T.C. Tsai, Modeling and Analysis of the Effects of Processing Parameters on the Performance Characteristics in the High Pressure Die Casting Process of Al-SI Alloys, *Int. J. Adv. Manuf. Technol.*, 2009, **41**(11), p 1076–1084

6. Y. Motoyama, H. Shiga, T. Sato, H. Kambe, and M. Yoshida, Elasto-Plastic-Creep Constitutive Equation of an Al-Si-Cu High-Pressure Die Casting Alloy for Thermal Stress Analysis, *Metall. Mater. Trans. A.*, 2016, **47**(11), p 5598–5608

7. P. Thasleem, D. Kumar, M.L. Joy, and B. Kuriachen, Effect of Heat Treatment and Electric Discharge Alloying on the Lubricated Tribology of Al-Si Alloy Fabricated by Selective Laser Melting, *Wear*, 2022, **494**, p 204244

8. P. Hofer, E. Kaschnitz, and P. Schumacher, Distortion and Residual Stress in High-Pressure Die Castings: Simulation and Measurements, *Jom*, 2014, **66**(9), p 1638–1646

9. J. Lee, Y. Eun Jeong, D. Sik Shim, and E. Lee, Microstructural Evolution and Martensitic Transformation in FeCrV Alloy Fabricated Via Additive Manufacturing, *Mater. Sci. Eng. A*, 2021, **809**, p 140943

10. Y. Liu, Y. Yang, and D. Wang, A Study on the Residual Stress During Selective Laser Melting (SLM) of Metallic Powder, *Int. J. Adv. Manuf. Technol.*, 2016, **87**(1), p 647–656

11. N.S. Rossini, M. Dassisti, K.Y. Benyounis, and A.G. Olabi, Methods of Measuring Residual Stresses in Components, *Mater. Des.*, 2012, **35**, p 572–588

12. T. Mukherjee, W. Zhang, and T. DebRoy, An Improved Prediction of Residual Stresses and Distortion in Additive Manufacturing, *Comput. Mater. Sci.*, 2017, **126**, p 360–372

13. S. Marola, S. Bosia, A. Veltro, G. Fiore, D. Manfredi, M. Lombardi, G. Amato, M. Baricco, and L. Battezzati, Residual Stresses in Additively Manufactured AlSi10Mg: Raman Spectroscopy and X-ray Diffraction Analysis, *Mater. Des.*, 2021, **202**, p 109550

14. A. Lombardi, D. Sediako, A. Machin, C. Ravindran, and R. MacKay, Effect of Solution Heat Treatment on Residual Stress in Al Alloy Engine Blocks Using Neutron Diffraction, *Mater. Sci. Eng. A*, 2017, **697**, p 238–247

15. L. Xie, C. Jiang, and V. Ji, Thermal Relaxation of Residual Stresses in Shot Peened Surface Layer of (TiB+ TiC)/Ti-6Al-4V composite at Elevated Temperatures, *Mater. Sci. Eng. A*, 2011, **528**(21), p 6478–6483

16. E. Lee, C. Walde, and B. Mishra, Effects of Cooling Rate on Precipitate Evolution and Residual Stresses in Al-Si-Mn-Mg Casting Alloy, *Met. Mater. Int.*, 2018, **24**(4), p 815–820

17. V. Sergo, G. Pezzotti, O. Sbaizero, and T. Nishida, Grain Size Influence on Residual Stresses in Alumina/Zirconia Composites, *Acta Mater.*, 1998, **46**(5), p 1701–1710

18. W. Węglewski, M. Basista, A. Manescu, M. Chmielewski, K. Pietrzak, and T. Schubert, Effect of Grain Size on Thermal Residual Stresses and

Damage in Sintered Chromium–Alumina Composites: Measurement and Modeling, *Compos. B Eng.*, 2014, **67**, p 119–124

19. A.K. Roy, S. Bandyopadhyay, S.B. Suresh, D. Maitra, P. Kumar, D. Wells, and L. Ma, Relationship of Residual Stress to Dislocation Density in Cold-Worked Martensitic Alloy, *Mater. Sci. Eng. A*, 2006, **416**(1–2), p 134–138

20. I. Rosenthal, R. Shneck, and A. Stern, Heat Treatment Effect on the Mechanical Properties and Fracture Mechanism in AlSi10Mg Fabricated by Additive Manufacturing Selective Laser Melting Process, *Mater. Sci. Eng. A*, 2018, **729**, p 310–322

21. F. Nazari, M. Honarpisheh, and H. Zhao, The Effect of Microstructure Parameters on the Residual Stresses in the Ultrafine-Grained Sheets, *Micron*, 2020, **132**, p 102843

22. A. Kumar. (2020). Estimation of crystallite size, lattice strain and micro residual stresses by FWHM method and impact of feed rates on residual stresses. In *IOP Conference Series: Materials Science and Engineering* Vol. 988. No. 1. IOP Publishing

23. M.E. Turan, F. Aydin, Y. Sun, and M. Cetin, Residual Stress Measurement by Strain Gauge and X-ray Diffraction Method in Different Shaped Rails, *Eng. Fail. Anal.*, 2019, **96**, p 525–529

24. Y. Saberi, S.M. Zebarjad, and G.H. Akbari, On the Role of Nano-Size SiC on lattice Strain and Grain Size of Al/SiC Nanocomposite, *J. Alloy. Compd.*, 2009, **484**(1–2), p 637–640

25. U. Scheuer and B. Lengeler, Lattice Distortion of Solute Atoms in Metals Studied by X-ray-Absorption Fine Structure, *Phys. Rev. B*, 1991, **44**(18), p 9883

26. T. Uesugi and K. Higashi, First-Principles Studies on Lattice Constants and Local Lattice Distortions in Solid Solution Aluminum Alloys, *Comput. Mater. Sci.*, 2013, **67**, p 1–10

27. Y. Jia, F. Cao, S. Scudino, P. Ma, H. Li, L. Yu, J. Eckert, and J. Sun, Microstructure and Thermal Expansion Behavior of Spray-Deposited Al-50Si, *Mater. Des.*, 2014, **57**, p 585–591

28. X.L. Zou, Y.A.N. Hong, and X.H. Chen, Evolution of Second Phases and Mechanical Properties of 7075 Al Alloy Processed by Solution Heat Treatment, *Trans. Nonferrous Met. Soc. China*, 2017, **27**(10), p 2146–2155

29. H.J. Bunge, Zur Darstellung Allgemeiner Texturen, *Int. J. Mater. Res.*, 1965, **56**(12), p 872–874

30. P.S.M. Jena, S.K. Pradhan, S. Tripathy, B. Mahato, C. Fernando, N. Paulose, and J.K. Sahu, A Selective Laser Melting and Solution Heat Treatment Refined Al-12Si Alloy with a Controllable Ultrafine Eutectic Microstructure and 25% Tensile Ductility, *Mater. Sci. Eng. A*, 2021, **807**, p 140855

31. J.F. Nye, Some Geometrical Relations in Dislocated Crystals, *Acta Metall.*, 1953, **1**(2), p 153–162

32. C. Fressengeas, B. Beausir, C. Kerisit, A.L. Helbert, T. Baudin, F. Brisset, M.H. Mathon, R. Besnard and N. Bozzolo, On the Evaluation of Dislocation Densities in Pure Tantalum from EBSD Orientation Data, *Matériaux Tech.*, 2018, **106**(6), p 604

33. X.P. Li, X.J. Wang, M. Saunders, A. Suvorova, L.C. Zhang, Y.J. Liu, M.H. Fang, Z.H. Huang, and T.B. Sercombe, A Selective Laser Melting and Solution Heat Treatment Refined Al-12Si Alloy with a Controllable Ultrafine Eutectic Microstructure and 25% tensile Ductility, *Acta Mater.*, 2015, **95**, p 74–82

34. B. Hengyong, L. Chen, and Y. Duan, Effect of Solution Heat Treatment on the Porosity Growth of Nickel-Based P/M Superalloys, *Metals*, 2022, **12**(11), p 1973. https://doi.org/10.3390/met12111973

35. Y. Yang, Y. Chen, J. Zhang, X. Gu, P. Qin, N. Dai, X. Li, J.P. Kruth, and L.C. Zhang, Improved Corrosion Behavior of Ultrafine-Grained Eutectic Al-12Si Alloy Produced by Selective Laser Melting, *Mater. Des.*, 2018, **146**, p 239–248

36. F. Alghamdi, X. Song, A. Hadadzadeh, B. Shalchi-Amirkhiz, M. Mohammadi, and M. Haghshenas, Post Heat Treatment of Additive Manufactured AlSi10Mg: On Silicon Morphology, Texture and Small-Scale Properties, *Mater. Sci. Eng. A*, 2020, **783**, p 139296

37. X. Zhu, R. Wang, C. Peng, W. Liu, and J. Peng, Microstructure and Thermal Expansion Behavior of Spray-Formed Al–27Si Alloy Used for Electronic Packaging, *J. Mater. Sci. Mater. Electron.*, 2014, **25**(11), p 4889–4895

38. R.J. Arsenault and N. Shi, Dislocation Generation due to Differences Between the Coefficients of Thermal Expansion, *Mater. Sci. Eng.*, 1986, **81**, p 175–187

39. N. Kang, P. Coddet, H. Liao and C. Coddet, Macrosegregation Mechanism of Primary Silicon Phase in Selective Laser Melting Hypereutectic Al–High Si alloy, *J. Alloy. Compd.*, 2016, **662**, p 259–262

40. A. Bendijk, R. Delhez, L. Katgerman, T.H. De Keijser, E.J. Mittemeijer, and N.M. Van Der Pers, Characterization of Al-Si-Alloys Rapidly Quenched from the Melt, *J. Mater. Sci.*, 1980, **15**(11), p 2803–2810

41. S. Marola, D. Manfredi, G. Fiore, M.G. Poletti, M. Lombardi, P. Fino, and L. Battezzati, A Comparison of Selective Laser Melting with Bulk Rapid Solidification of AlSi10Mg Alloy, *J. Alloy. Compd.*, 2018, **742**, p 271–279

42. H. Zhang, D. Gu, D. Dai, C. Ma, Y. Li, R. Peng, S. Li, G. Li, and B. Yang, Influence of scanning strategy and parameter on microstructural feature, residual stress and performance of Sc and Zr modified Al-Mg alloy produced by selective laser melting, *Mater. Sci. Eng. A*, 2020, **788**, p 139593

43. V. Mote, Y. Purushotham, and B. Dole, Williamson-Hall Analysis in Estimation of Lattice Strain in Nanometer-Sized ZnO Particles, *J. Theoret. Appl. Phys.*, 2012, **6**(1), p 1–8

44. C.E. Krill and R. Birringer, Estimating Grain-Size Distributions in nanocrystalline Materials from X-ray Diffraction Profile Analysis, *Philos. Mag. A*, 1998, **77**(3), p 621–640

45. R.S. Lei, M.P. Wang, Z. Li, H.G. Wei, W.C. Yang, and Y.L. Jia, Structure Evolution and Solid Solubility Extension of Copper–Niobium Powders During Mechanical Alloying, *Mater. Sci. Eng. A*, 2011, **528**(13–14), p 4475–4481

46. Z. Wei, P. Ma, H. Wang, C. Zou, S. Scudino, K. Song, K.G. Prashanth, W. Jiang, and J. Eckert, The Thermal Expansion Behaviour of SiCp/Al–20Si Composites Solidified Under High Pressures, *Mater. Des.*, 2015, **1980–2015**(65), p 387–394

47. Y.D. Jia, P. Ma, K.G. Prashanth, G. Wang, J. Yi, S. Scudino, F.Y. Cao, J.F. Sun, and J. Eckert, Microstructure and Thermal Expansion Behavior of Al-50Si Synthesized by Selective Laser Melting, *J. Alloy. Compd.*, 2017, **699**, p 548–553

48. Y.D. Jia, L.B. Zhang, P. Ma, S. Scudino, G. Wang, J. Yi, J. Eckert, and K.G. Prashanth, Thermal Expansion Behavior of Al-xSi Alloys Fabricated Using Selective Laser Melting, *Progr. Addit. Manuf.*, 2020, **5**(3), p 247–257